Available online at www.sciencedirect.com
SCIENCE DIRECT®
Journal of Sound and Vibration 285 (2005) 835–857
JOURNAL OF SOUND AND VIBRATION
www.elsevier.com/locate/jsvi

Full waveform inversion of a 3-D source inside an artificial rock

Albert C. To[a,b], Steven D. Glaser[a,b,*]

[a]*Center for Information Technology Research in the Interest of Society, University of Berkeley, Berkeley, CA, USA*
[b]*281 Hearst Memorial Mining Building, Berkeley, CA 94120-1761, USA*

Received 3 March 2004; received in revised form 18 August 2004; accepted 31 August 2004
Available online 18 December 2004

Abstract

A full waveform inversion of the kinematics of a 3-D source inside an artificial rock plate is presented. The source is provided by a piezoelectric disc embedded inside a gypsum plate, excited by an arbitrary electrical signal. Elastic waves emitted from the source propagated through the plate and were recorded by an array of wide-band high-fidelity microseismic displacement sensors. These microseismic data are then inverted by deconvolving the recorded signals with the theoretical Green's functions to obtain the kinematics of the source modeled by force couples. The force time functions thus inverted are justified qualitatively by the known mechanical behavior and compared quantitatively to simplified electro-acoustic equations. For the first time, the combined use of a wide-band high-fidelity sensor, Green's functions incorporating Q damping, effective point source theory, and linear deconvolution yield physically justified time functions of the source kinematics.

1. Introduction

Determination of the kinematics of crack growth is of great importance in engineering and science. The kinematics of a source within a solid can in theory be estimated by inverting recorded microseismic (MS) signals generated by the source. In the present paper, a full waveform inversion

*Corresponding author. Center for Information Technology Research in the Interest of Society, University of Berkeley, Berkeley, CA 94122, USA. Tel.: +1 510 642 1264; fax: +1 510 642 7476.
E-mail address: glaser@ce.berkeley.edu (S.D. Glaser).

0022-460X/$ - see front matter © 2004 Elsevier Ltd. All rights reserved.
doi:10.1016/j.jsv.2004.09.001

of the kinematics of a 3-D source inside an artificial rock plate is presented. The 3-D source is a piezoelectric disc that expands (or contracts) in the axial direction and contracts (or expands) in the radial direction due to the input of an arbitrary electric signal.

Inversion methods can be generally divided into three categories: (1) inversion by use of only the initial *p*-wave amplitude, (2) full waveform inversion by empirical Green's function, and (3) full waveform inversion by theoretical Green's function. In the first category, only the amplitude of the first *p*-wave pulse is used to determine the type of crack and the size of the source [1–3]. This method will lead to an answer very quickly and does not require the use of Green's functions, but it does not give the complete behavior of the crack as a function of time.

In the second category, the MS signals are inverted from an empirical Green's function to obtain time function of the kinematics [4–6]. The resulting source time function is very accurate because the empirical Green's function accounts for the receiver transfer function and anelasticity which arises from crystal defects, grain-boundary processes, and viscoelasticity, which are difficult to account for individually when calculating a theoretical Green's function. However, obtaining the empirical Green's function is practically impossible inside a solid without disturbing the solid (except when the source is a monopole on the surface of a solid).

In the third category, the MS signals are inverted from the calculated theoretical Green's functions to obtain the kinematics of the source [7]. The most direct inversion method is by direct linear deconvolution of the MS data from the calculated Green's functions [8,9]. The linear deconvolution method can be used to invert for sources of any nature and location, but the success of this method hinges on (1) how close the solid model used to calculate the Green's function is to the actual physical properties of the solid, and (2) the estimation of the transfer function of the transducer. Errors in the Green's function and the transducer transfer function are projected onto the resulting source time functions and render them physically unjustified. Very few works to date have applied this method successfully to MS data. Kim and Sachse [10,11] presented a full waveform inversion of indentation cracks and thermal cracks in glass, respectively. In Enoki and Kishi [12], recorded signals due to cracks were inverted to give the source time function for a fracture toughness testing in steel. Shah and Labuz [13] studied the damage mechanisms in stressed rock by performing full waveform inversion. In these works, the material is assumed to be elastic, isotropic, and homogeneous, while the source is assumed to be a point source.

Because of the difficulty of obtaining physically justified source time functions by linear deconvolution, the source time function is usually parameterized a *priori* to constrain the solution space, which is routinely performed by seismologists and acoustic emission practitioners nowadays [7,14]. The most common parameterization of the source time function consists of assuming a certain waveform with parameters of rise time and amplitude of the first motion. This method is accurate when the waveform of the source process is known, i.e., the source time function of a dynamic mode I crack is a step function, but this method will not work for a complicated source. Another disadvantage associated with parameterization of the source time function is that the inversion problem becomes nonlinear and will always involve more complicated algorithms to solve the problem [15,16].

In this study, high-fidelity sensors with flat frequency response are used to record the MS data so that the estimation of the sensor transfer function is not needed for inversion [17]. Green's functions that incorporate attenuation in the material, which is realistic for rocks, are employed to

give accurate results [22]. The finiteness of the dimension of the source is also considered, i.e. the whole source region is discretized into subregions such that each subregion satisfies the effective point source criterion [7]. The recorded data are inverted by direct linear deconvolution and the inverted results are compared qualitatively to the known mechanical behavior and compared quantitatively to the simplified electro-acoustic equations of piezoelectrics. Although the use of high-fidelity sensors, the calculation of the Green's function that includes damping, the summation of point sources into a finite source, and the direct linear deconvolution are each not new, the incorporation of all of the above to obtain physically justified source time functions for a finite complex source is a new development in MS inversion.

2. Experimental setup

To model a realistic source, a ceramic disc (PZT-5A, Vernitron) of 13.45 mm diameter and 7.16 mm thickness is embedded inside a $850 \times 850 \times 42\,\text{mm}^3$ gypsum plate, at a vertical distance of 15.7 mm from the top surface of the plate (Fig. 1). The disc expands (or contracts) in the axial direction parallel to the plate surface due to the input of an electric signal and correspondingly contracts (or expands) in the radial direction (Fig. 2). The source is known to resonate, and the signal is highly reproducible. The gypsum plate is made out of a ready-mix dry powder called Die-Keen from Modern Materials, and is chosen because of its desirable physical properties for modeling. First, the powder is manufactured in a finely ground state so that the plate thus formed is very homogeneous. Second, it is as strong as competent natural intact rock. Third, it exhibits only 0.41% expansion after setting, such that the residual stresses are small and shrinkage cracks are not likely to form. Some physical properties of PZT-5A and the gypsum plate are listed in

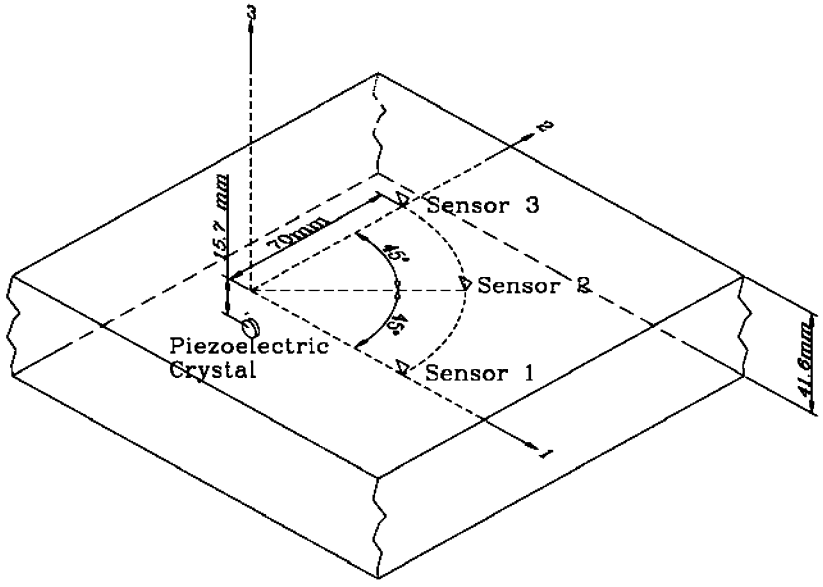

Fig. 1. Gypsum test plate with a piezoelectric disc embedded inside and sensors on the top surface.

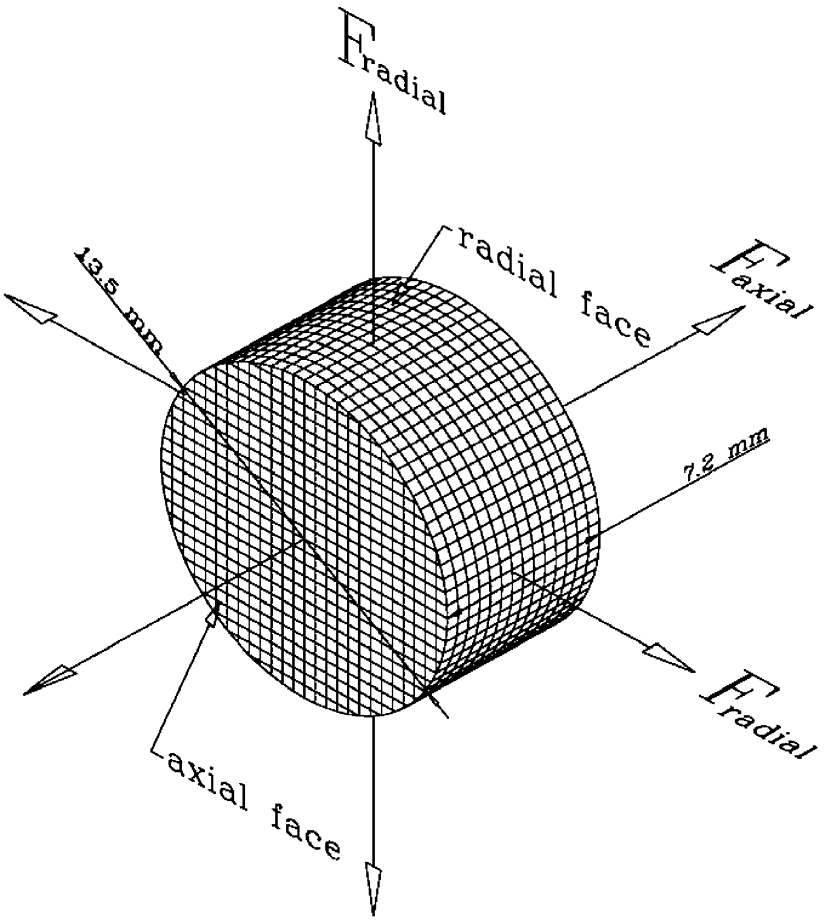

Fig. 2. Orientation of the 3-D source discretization of the source into sub-regions for calculation of Green's functions.

Table 1. As will be discussed, the known mechanical properties of the disc and the gypsum are important not only for formulating the inverse problem, but also for interpreting the resulting time function of the kinematics obtained from the inversion.

High-fidelity, wide band transducers sensitive to displacement normal to the monitored interface are used for this experiment because this provides a time history of surface displacement without the distortion of the waveform [17]. For sensors that are narrow band, the transfer function of the sensor needs to be estimated and the recorded displacements by the sensor need to be deconvolved from its transfer function [4], and frequencies not recorded cannot ever be recovered by any means. On the other hand, the sensors we use have a flat response from 12 kHz to 1 MHz, so only the sensitivity (in V/m) needs to be calculated and absolute displacement is easily obtained [17]. The sensitivity of the transducer is estimated by a capillary break procedure developed in Ref. [4]. For the surface-mounted sensors used in this experiment, the sensitivity was 2.8 V/nm [17].

Table 1
Physical properties of the PZT-5A disc and the gypsum plate

	PZT-5A	Gypsum plate
Density ρ (10^3 kg/m^3)	7.75	2.6
p-wave velocity V_p (10^3 m/s)	3.78[E], 4.36[C]	4.23
s-wave velocity V_s (10^3 m/s)	—	2.35
Q_p	—	70
Q_s	—	29
Piezoelectric constants (10^{-12} m/V)		
d_{31}	−171	—
d_{33}	374	—
d_{15}	584	—
Elastic compliance at constant electric field (10^{-12} m^2/N)		
s_{11}^E	16.4	—
s_{33}^E	18.8	—
s_{44}^E	47.5	—
s_{12}^E	−5.74	—
s_{13}^E	−7.22	—
Elastic compliance at constant charge density (10^{-12} m^2/N)		
s_{11}^D	14.4	—
s_{33}^D	9.46	—
s_{44}^D	25.2	—
s_{12}^D	−7.71	—
s_{13}^D	−2.98	—

[E]Axial p-wave velocity measured at constant electric field.
[C]Axial p-wave velocity measured at constant charge density.

As illustrated in Fig. 1, three sensors are placed on the top surface of the plate in a radial pattern, 45° apart from each other and at a radial distance of 70 mm from the source. The axial direction of the source lines up with Sensor 3. The transient responses due to the excitation of the source are digitally sampled at a 0.2 μs interval at 14-bit resolution.

In the experiment, the PZT disc is mechanically deformed by inputting an electric signal and the elastic waves emitted and propagated through the gypsum plate are received by the transducers. The input electric signal is a single cycle sinusoidal wave because of its simplicity and also because the resonant behavior of the disc can be observed and analyzed after the input signal becomes zero. A variety of signals having peak-to-peak voltage of 1 kV and bandpassed between 50 kHz and 20 MHz, but with different center frequencies, is tested. The input signals of center frequencies of 400 kHz, 600 kHz, 800 kHz, and 1 MHz are shown in Fig. 3. An example of the time-displacement waveforms recorded due to the 400 kHz central frequency source is shown in Fig. 4. The first p-wave arrives at 0 μs, but the energy from the first p-wave arrival is concentrated between 3.5 and 6 μs followed by *pp*, *ppp*, *ps*, and *sp* arrivals. The first shear wave energy is concentrated between 19 and 21 μs, but it cannot be clearly discerned because it is blurred by the

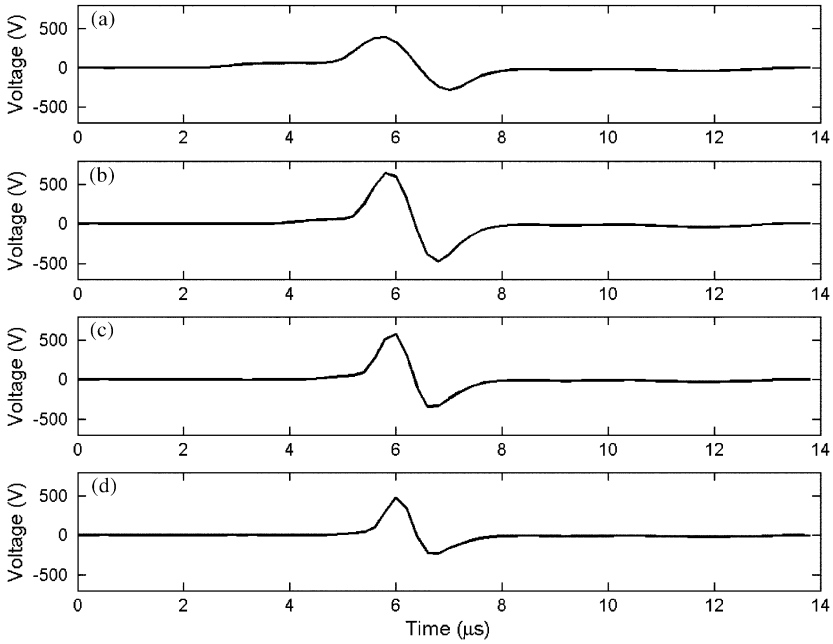

Fig. 3. Input electric signals of single-cycle sinusoidal functions to the piezoelectric disc with various central frequencies: (a) 400 kHz, (b) 600 kHz, (c) 800 kHz, and (d) 1 MHz.

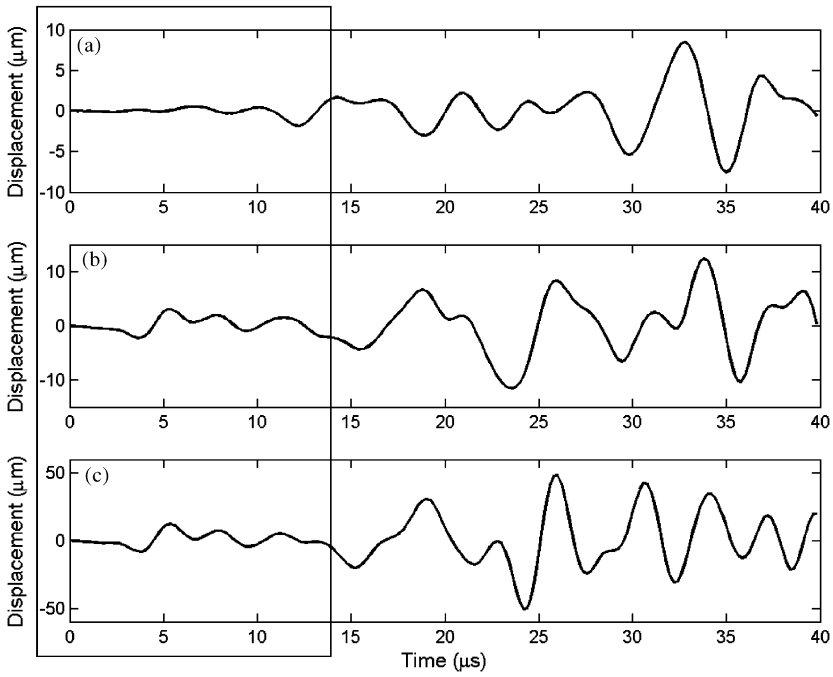

Fig. 4. An example set of time–displacement signals recorded on plate surface for the electric signal with central frequency of 400 kHz in Fig. 3a. Only the windowed data are used for inversion to determine the source time function. (a) sensor 1, (b) 2, (c) 3.

ps and *sp* wave energies. The energy from the Rayleigh wave is concentrated between 23 and 27 μs. A time window of first 14 μs after the first *p*-wave arrival is used for inversion for the source time function (Fig. 4). As just discussed, this time window includes the *p*, *pp*, *ppp*, *ps*, and *sp* wave arrivals. In the experimental setup, the distance from the source to the closest edge of the plate is 254 mm, and so the first reflection off the edge is 44 μs after the first *p*-wave arrival. The wave arrives at the edge long after the cutoff time in the inversion, and thus has little effect on the waveform under consideration. Also, the edge effect on the waveform before the wave reflects off the edge was shown to be insignificant by Micheals et al. [5], and others [6].

3. The forward problem

The kinematics of a point source can be completely described by a linear combination of nine force couples or moments (three components of force and three components of arm directions) as shown in Fig. 5 [18]. Literally, the moment tensor $M_{pq}(\xi,t)$ is defined as the limit of the product of the the qth direction force arm $\Delta\xi_q$ and the pth direction forcing function $F_p(\xi,t)$ at location ξ and time t [18]:

$$M_{pq}(\xi,t) = \lim_{\substack{\Delta\xi_q \to 0 \\ F_p \to \infty}} \Delta\xi_q F_p(\xi,t), \tag{1}$$

where F_p is the force time function in the pth direction and $\Delta\xi_q$ is the force arm in the qth direction. The moment tensor $M_{pq}(\xi,t)$ is symmetric in p and q due to the conservation of momentum for an internal source [18], and thus there are six unique moments instead of nine. The displacement time history $u_n(\mathbf{x},t)$ at location $\mathbf{x}$ in the nth direction due to a point source can be

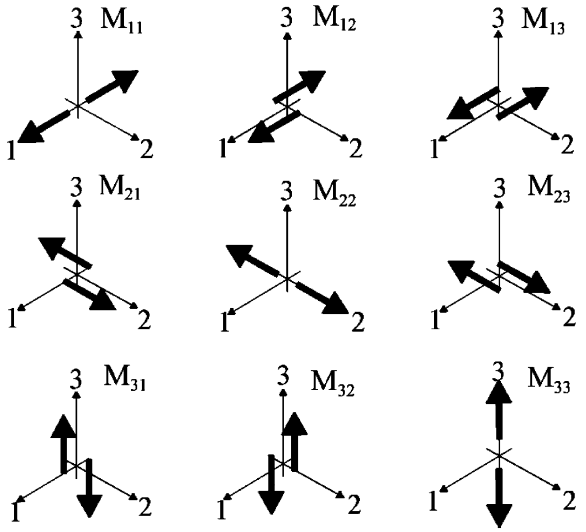

Fig. 5. Nine components of the moment tensor (Aki and Richards, [18]).

modeled as a convolution integral of the moment tensor and the Green's displacement tensor:

$$u_n(\mathbf{x},t)=\sum_{p=1}^{3}\sum_{q=1}^{3}G_{np,q}(\mathbf{x},t;\xi,0)*M_{pq}(\xi,t), \tag{2}$$

where an asterisk denotes a convolution integral in the time variable. The Green's displacement tensor $G_{np,q}(\mathbf{x},t,\xi,0)$ is the displacement in the nth direction at $\mathbf{x}$ and t due to a unit impulsive concentrated moment at ξ and $t=0$.

Unfortunately, instead of being point sources, cracks have a real extent and the time history of the growing crack is of primary interest. For a source over a finite area A, the displacement at location $\mathbf{x}$ in the nth direction can be obtained by integrating Eq. (2) over A:

$$u_n(\mathbf{x},t)=\iint_{\Sigma}\sum_{p=1}^{3}\sum_{q=1}^{3}G_{np,q}(\mathbf{x},t;\xi,0)*M_{pq}(\xi,t)\,dA. \tag{3}$$

According to Johnson and Stump [7], if the region A is discretized into N_r sub-regions whose largest dimension is smaller than the smallest wavelength of interest, each sub-region i is well approximated by a point source. Therefore, summing the contribution from the sub-regions, we obtain

$$u_n(\mathbf{x},t)=\sum_{i=1}^{N_r}\sum_{p=1}^{3}\sum_{q=1}^{3}G_{np,q}(\mathbf{x},t;\xi^{(i)},0)*M_{pq}(\xi^{(i)},t). \tag{4}$$

So far, we have focused on modeling the kinematics of a source whose volume is infinitesimal, but the volume of the actual simulated crack in the experiment is not, and thus the force arm in Eq. (1) is no longer infinitesimal. Eq. (4) can be first rewritten as

$$u_n(\mathbf{x},t)=\sum_{i=1}^{N_r}\sum_{p=1}^{3}\sum_{q=1}^{3}\left(\lim_{\Delta\xi_q^{(i)}\to 0}\frac{G_{np}(\mathbf{x},t;\xi^{(i)}+0.5\Delta\xi_q^{(i)},0)-G_{np}(\mathbf{x},t;\xi^{(i)}-0.5\Delta\xi_q^{(i)},0)}{\Delta\xi_q^{(i)}}\right.$$
$$\left.\lim_{\substack{\Delta\xi_q^{(i)}\to 0\\ f_p\to\infty}}\Delta\xi_q^{(i)}F_p(\xi^{(i)},t)\right) \tag{5}$$

and then removing the limits from Eq. (5), we obtain

$$u_n(\mathbf{x},t)=\sum_{i=1}^{N_r}\sum_{p=1}^{3}\sum_{q=1}^{3}\left((G_{np}(\mathbf{x},t;\xi^{(i)}+0.5\Delta\xi_q^{(i)},0)-G_{np}(\mathbf{x},t;\xi^{(i)}-0.5\Delta\xi_q^{(i)},0))*F_p(\xi^{(i)},t)\right) \tag{6}$$

where $G_{np}(\mathbf{x},t;\xi^{(i)},0)$ is the displacement in the nth direction at $\mathbf{x}$ and t due to a unit impulsive concentrated force at $\xi^{(i)}$ and $t=0$. $F_p(\xi^{(i)},t)$ is the force time function in the pth direction. Eq. (6)

can be interpreted as the sum of the displacements due to time-variant force couples with finite moment arms on all the sub-regions.

4. Calculation of Green's functions

The Green's functions for an isotropic, homogeneous infinite plate with constant Q damping law by Kjartansson [19] due to a point source is calculated by the frequency–wavenumber method by Kennett [20]. In this method, the equation of motion is transformed into the frequency–wavenumber domain for ease of manipulation. The resulting solution is a frequency–wavenumber integral, which is solved numerically. The computation time needed for the Green's functions calculated by the frequency–wavenumber method is faster than numerical methods such as finite difference and finite elements [20].

4.1. Determination of Q

The dimensionless quality factor Q accounts for various damping mechanisms, and is effectively constant over a wide range of frequencies for many geological materials [22]. These damping mechanisms include crystal defects, grain boundary processes, microcracks, and viscoelastic processes, which are all interrelated. Q decreases as the number of cracks and crack sizes increase and as the material has higher damping, so when Q decreases, the attenuation of propagating waves increases. The recorded phase amplitude $A(f)$ of a wave by a sensor propagating in a constant Q damping material is [21]

$$A(f) = I(f)S(f)G(t)\ \exp\left(-\frac{\pi f t}{Q}\right), \tag{7}$$

where f is the frequency, $I(f)$ is the sensor transfer function, $S(f)$ is the source function and t is the time the wave has travelled. $G(t)$ represents frequency-independent processes that affect the wave along its propagation path, such as geometrical spreading and reflection and transmission at boundaries without phase shift. As will be seen below, only the exponential term in Eq. (7) is important in determining Q, i.e. the relative change in attenuation of a wave over a wide range of frequencies is desired, and so a wide band source will serve this purpose.

For a plate of a given material, the dimensionless quality factor Q for the p-wave (Q_p) can be determined by estimating the spectral ratio of a signal generated by breaking a glass capillary on the opposite side of the plate relative to the sensor. The capillary break is generated by loading a rod vertically on a glass capillary placed flat on the plate until the capillary shatters suddenly [4]. Before the capillary breaks, the plate is displaced locally by the vertical force exerted by the rod through the capillary. Once the capillary breaks, the surface displacement recovers suddenly. This sudden rebound generates a step-like function that has a very short rise time. Since the capillary break is a wide band source from DC to well above 1 MHz [4], it is a good source to use for estimating Q.

Now consider the spectral ratio

$$R(f) = \frac{A_{ppp}(f)}{A_p(f)}, \tag{8}$$

where $A_p(f)$ is the amplitude of the p phase in the frequency (f) domain and $A_{ppp}(f)$ is the amplitude of the reflected p phase. Substituting Eq. (7) into Eq. (8) gives

$$R(f) = \frac{G_p(t_p)\ \exp(-\pi f t_p/Q_p)}{G_{ppp}(t_{ppp})\ \exp(-\pi f t_{ppp}/Q_p)}. \tag{9}$$

Notice that both the sensor transfer function and the source function are cancelled. Taking the natural logarithm of Eq. (9) gives

$$\ln\ R(f) = \ln\left(\frac{G_p(t_p)}{G_{ppp}(t_{ppp})}\right) - \pi\Delta t/Q_p f, \tag{10}$$

where Δt is the time difference between the p phase arrival and the ppp phase arrival. From Eq. (10) Q_p can be estimated from the slope of $\ln(R(f))$ vs. f plot. The time derivative of the epicentral displacement from the average of three glass capillary breaks on the gypsum plate is plotted in Fig. 6. The time derivative of the epicentral displacement is used rather than the original signal because the p and the ppp phases can be observed and extracted easily from the signal. Also, note that Eq. (10) is still valid, since taking the time derivative is equivalent to multiplying the original signal by $i2\pi f$ in the frequency domain, and the factors for the p amplitude and the ppp amplitude cancel each other in Eq. (8). The natural log of the spectral ratio $R(f)$ of the p and the ppp phases as a function of frequency f is plotted in Fig. 7. Q_p is estimated to be 70 from linear regression fitting of a straight line through the $\ln(R(f))$ vs. f plot, and it is a typical value for natural rocks [22].

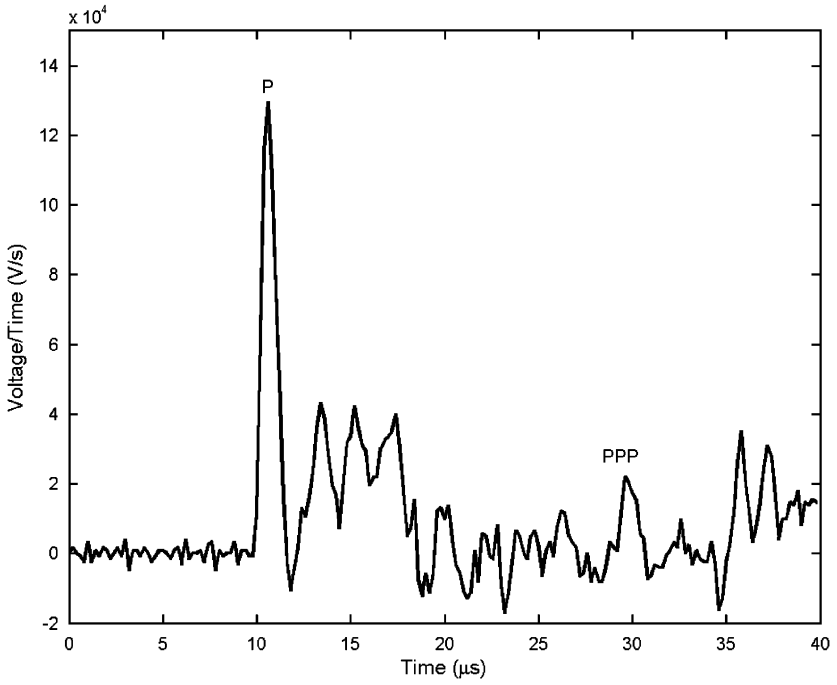

Fig. 6. Time derivative of the epicentral displacement due to a glass capillary break. The p and ppp phases are indicated in the figure.

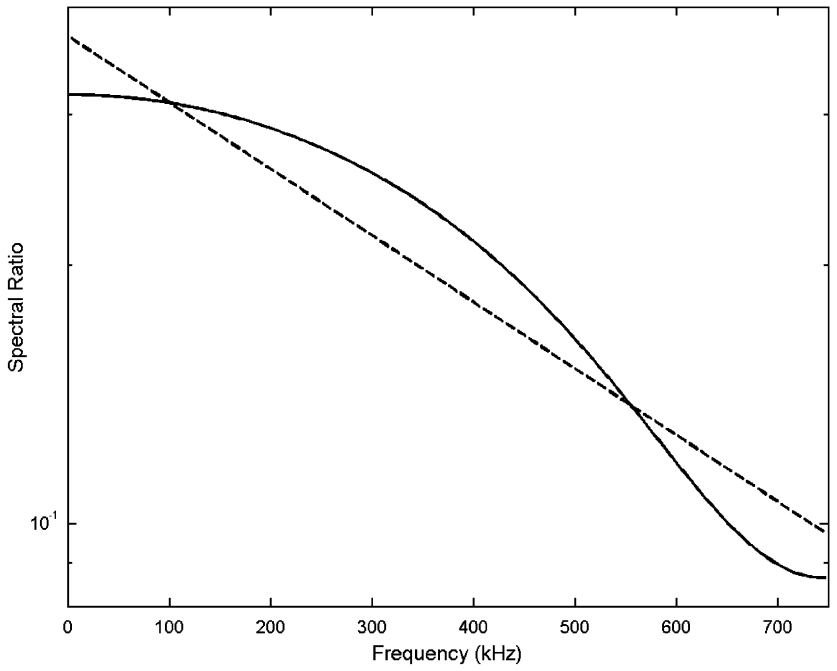

Fig. 7. The spectral ratio of the *ppp* and *p* phases (solid line) and the linear regression line from which q_p is estimated (dashed line).

In principle, the same technique above can be used to estimate Q for the shear wave (Q_s), i.e. by replacing the subscript p with s and *ppp* with *sss* in Eqs. (8)–(10). However, the reflected *sss* amplitude is very small due to the radiation pattern and is dominated by the p reflections and noise, so it is impractical to use this technique. However, assuming that no energy dissipation occurs in pure compression for the p-wave, Q_s can be estimated from Q_p by Apsel [23]:

$$Q_s = \frac{4}{3}\left(\frac{V_s}{V_p}\right)^2 Q_p, \tag{11}$$

where V_p and V_s are the respective p-wave and s-wave velocity.

It is simple to include Q damping in the calculation of the Green's functions by making the p-wave velocity (V_p) and s-wave velocity (V_s) complex [19]:

$$V = (V_0)\ \cos\left(\frac{\pi\gamma}{2}\right)\left(-\frac{\mathrm{i}\omega}{\omega_0}\right)\gamma \tag{12}$$

with

$$\gamma = \frac{1}{\pi}\arctan\left(\frac{1}{Q}\right), \tag{13}$$

where V is the p-wave or the s-wave velocity. V_0 is the reference velocity at frequency ω_0.

5. The inverse problem

The goal of the present study is to determine the force time function $F_p(\xi^{(i)},t)$ in Eq. (6) given several displacement time histories $u_n(\mathbf{x},t)$, Green's functions $G_{np}(\mathbf{x},t;\xi^{(i)},0)$, and the source location. In order to formulate the inverse problem for the experiment, the source needs to be discretized into sub-regions where each subregion is much less than the shortest wavelength of interest to be considered a point source effectively [7]. The axial face of the disc is discretized into mostly square sub-regions by 26 equally spaced vertical and horizontal lines, and the largest dimension of each sub-region is 0.52 mm. (Fig. 2). The radial face is discretized into 1120 sub-regions whose largest dimension is 0.53 mm. Each sub-region is now effectively a point source and thus the Green's functions for each sub-region can be calculated by the frequency–wavenumber method [20]. For the inverse problem, the unknown force time function of each direction for each sub-region needs to be determined, and that means thousands of sensor signals are needed to perform the inversion. However, the number of unknowns can be reduced substantially by applying our knowledge of the mechanical behavior of the PZT disc and the gypsum plate. The following two simplifications are made in the formulation of the inverse problem:

(1) Each subregion on the axial face can only exert an axial force and each subregion on the radial face can only exert a radial force.
(2) The axial force time function is identical for each subregion on the axial face and the radial force time function is identical for each subregion on the radial face.

These simplifications follow directly from the assumption that the bonding between the PZT disc and the gypsum is smooth (ie. frictionless) and that the disc expands (or contracts) in the axial direction due to the input of an electric signal and correspondingly contracts (or expands) in the radial direction. With the first simplication, the Green's function due to an impulsive axial force for each sensor (G_{axial} $(\mathbf{x},t;\xi,0)$) is calculated for each subregion on the axial face, and in the same manner, the Green's function due to an impulsive radial force for each sensor (G_{radial} $(\mathbf{x},t;\xi,0)$ is calculated for each subregion on the radial face. The set of equations to be solved can be written as

$$u_n(\mathbf{x}^{(j)},k) = \sum_{a=1}^{N_a}\left(G_{\text{axial}}(\mathbf{x}^{(j)},k;\xi^{(a)},0)\,F_{\text{axial}}(\xi^{(a)},k)\right) + \sum_{r=1}^{N_r}\left(G_{\text{radial}}(\mathbf{x}^{(j)},k;\xi^{(r)},0)\,F_{\text{radial}}(\xi^{(r)},k)\right),\quad j=1,2,...,N_s;k=0,1,...,N_t \tag{14}$$

where $\mathbf{x}^{(j)}$ is the jth sensor location, N_s is the number of sensors, N_a the number of sub-regions on the axial face, and N_r the number of subregions on the radial face. Since the observed displacements are discretized at an interval Δt, the continuous time t in Eq. (6) is replaced by increment k times Δt. F_{axial} $(\xi^{(a)},k)$ and F_{radial} $(\xi^{(r)},k)$ are the axial and radial force time functions at each subregion on the axial and radial face, respectively. With the second simplification that the force time function is identical for all the axial subregions and for all the radial subregions, respectively, the axial and the radial force time functions in Eq. (14) can be taken out of the

parentheses as follows:

$$u_n(\mathbf{x}^{(j)},k)=\sum_{a=1}^{N_a}\left(G_{\text{axial}}(\mathbf{x}^{(j)},k;\xi^{(a)},0)\right)F_{\text{axial}}(k)+\sum_{r=1}^{N_r}\left(G_{\text{radial}}(\mathbf{x}^{(j)},k;\xi^{(r)},0)\right)F_{\text{radial}}(k),\quad j=1,2,...,N_s,k=0,1,...,N_t. \tag{15}$$

Now, only two unknown force time functions $F_{\text{axial}}(k)$ and $F_{\text{radial}}(k)$ need to be determined, and with three sensor recordings from each test, the inverse problem is overdetermined. The force time functions in Eq. (15) are deconvolved in the time domain by the least-squares method. It is more convenient to write Eq. (15) in matrix notation:

$$\begin{bmatrix}\mathbf{u}_1\\ \vdots\\ \mathbf{u}_n\end{bmatrix}_{nN_t\times 1}=\begin{bmatrix}(\mathbf{G}_{\text{axial}})_1 & (\mathbf{G}_{\text{radial}})_1\\ \vdots & \vdots\\ (\mathbf{G}_{\text{axial}})_n & (\mathbf{G}_{\text{radial}})_n\end{bmatrix}_{nN_t\times 2N_t}\begin{bmatrix}\mathbf{F}_{\text{axial}}\\ \mathbf{F}_{\text{radial}}\end{bmatrix}_{2N_t\times 1}. \tag{16}$$

Consequently, the axial and radial force time functions can be obtained by standard least squares for $n>2$:

$$\begin{bmatrix}\mathbf{F}_{\text{axial}}\\ \mathbf{F}_{\text{radial}}\end{bmatrix}=\left(\begin{bmatrix}(\mathbf{G}_{\text{axial}})_1 & (\mathbf{G}_{\text{radial}})_1\\ \vdots & \vdots\\ (\mathbf{G}_{\text{axial}})_n & (\mathbf{G}_{\text{radial}})_n\end{bmatrix}^{\mathrm{T}}\begin{bmatrix}(\mathbf{G}_{\text{axial}})_1 & (\mathbf{G}_{\text{radial}})_1\\ \vdots & \vdots\\ (\mathbf{G}_{\text{axial}})_n & (\mathbf{G}_{\text{radial}})_n\end{bmatrix}\right)^{-1}\begin{bmatrix}(\mathbf{G}_{\text{axial}})_1 & (\mathbf{G}_{\text{radial}})_1\\ \vdots & \vdots\\ (\mathbf{G}_{\text{axial}})_n & (\mathbf{G}_{\text{radial}})_n\end{bmatrix}^{\mathrm{T}}\begin{bmatrix}\mathbf{u}_1\\ \vdots\\ \mathbf{u}_n\end{bmatrix}. \tag{17}$$

In this study, the Green's function for each subregion and sensor takes 10 min to compute on a 900 MHz Intel Pentium III processor with 500 mb memory. A total of 6768 Green's functions were calculated in 47 days of time. The axial and radial Green's functions used for the inversion are shown in Figs. 8 and 9. Seventy time steps were used in the inversion for each electric input signal, and their estimates are shown in Figs. 10–13 along with their Fourier spectra.

6. Discussion

The most direct method to validate the inverted force time functions is to have a forward model for the PZT disc embedded inside the gypsum plate. Direct calculation of the force field in the whole solid due to an input electric signal that excites the PZT disc is well beyond the scope of this study. Rather, the force time functions are compared qualitatively to the known mechanical behavior and compared quantitatively to the simplified electro-acoustic equations.

As discussed earlier, the general mechanical behavior of the PZT disc is that it contracts (or expands) in the radial direction when it expands (or contracts) in the axial direction. It can be clearly seen that for each frequency excitation, the force time functions F_{axial} and F_{radial} are 180° out of phase. Also, since the disc is excited in the axial direction and the axial face is larger than

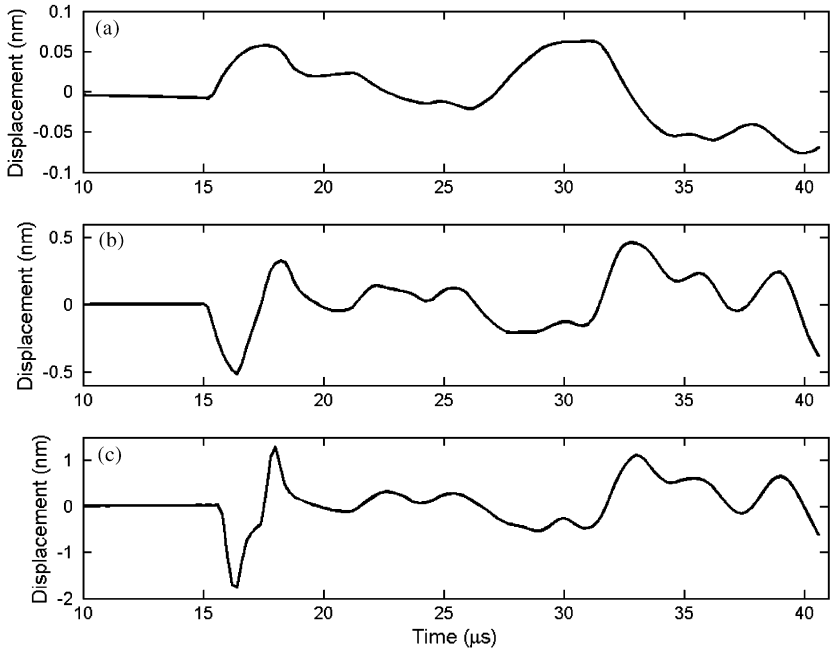

Fig. 8. Green's functions in the axial direction corresponding to (a) sensor 1, (b) 2, and (c) 3.

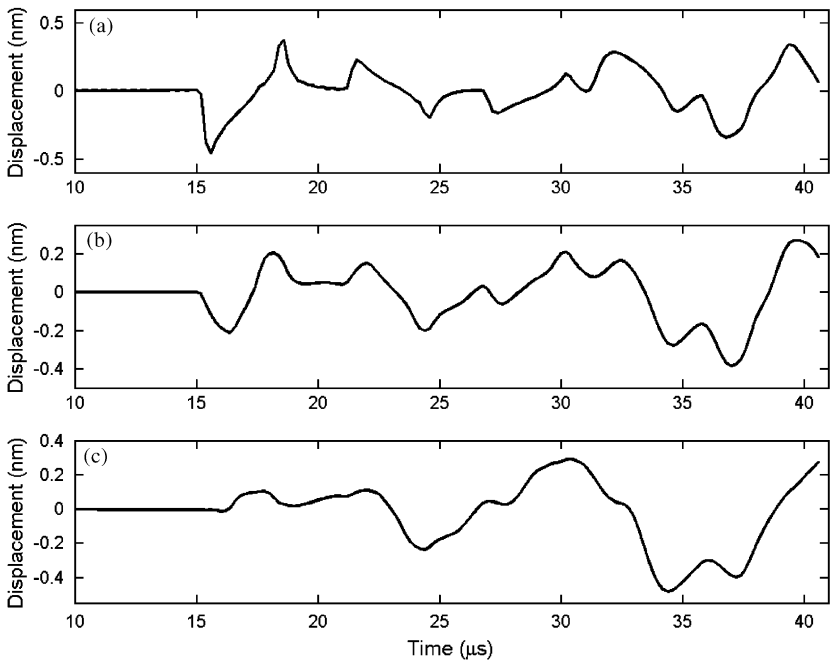

Fig. 9. Green's functions in the radial direction corresponding to (a) sensor 1, (b) 2, and (c) 3.

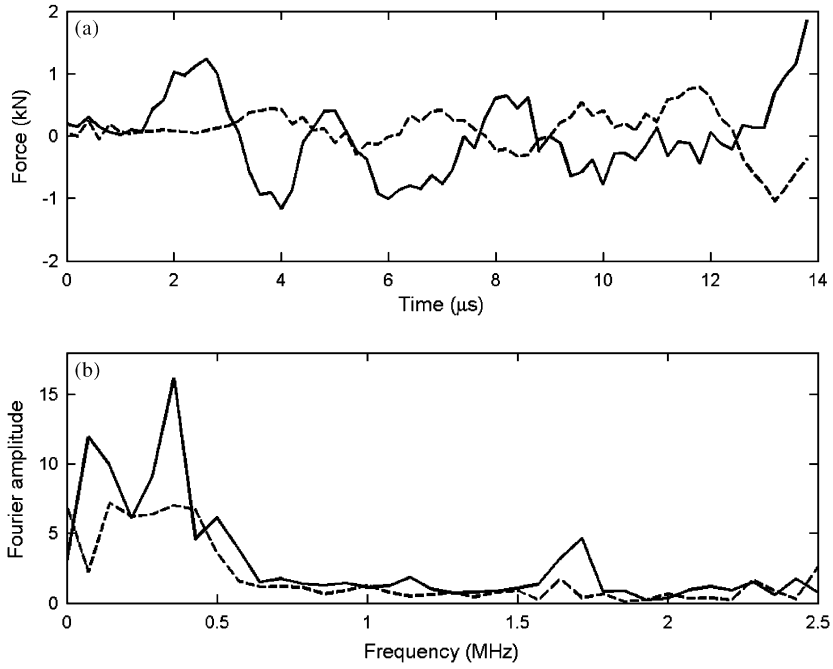

Fig. 10. (a) The force time function of the 3-D source due to the input signal with central frequency of 400 kHz and (b) the Fourier spectrum of the force time function; ——, axial; - - -, radial.

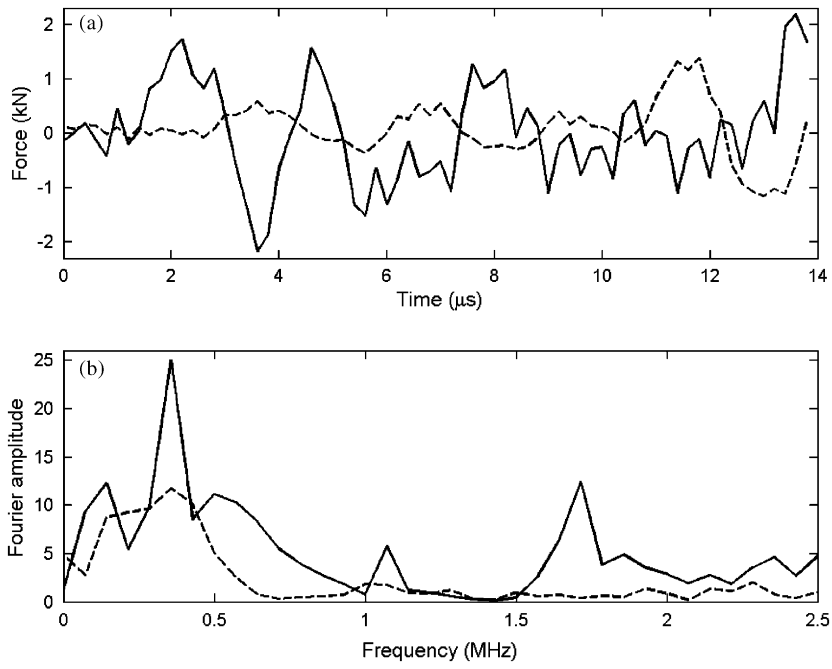

Fig. 11. (a) The force time function of the 3-D source due to the input signal with central frequency of 600 kHz and (b) the Fourier spectrum of the force time function; ——, axial; - - -, radial.

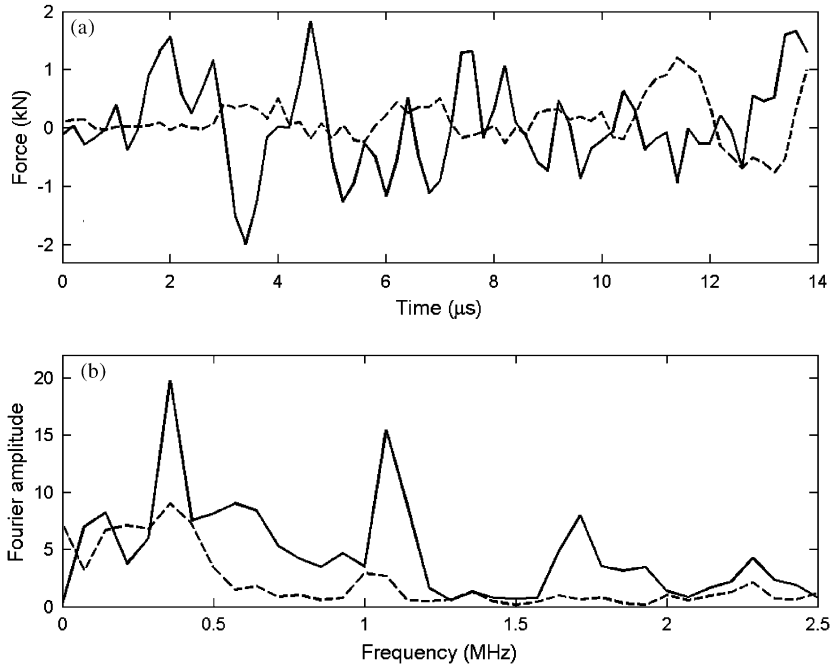

Fig. 12. (a) The force time function of the 3-D source due to the input signal with central frequency of 800 kHz and (b) the Fourier spectrum of the force time function; ——, axial; - - -, radial.

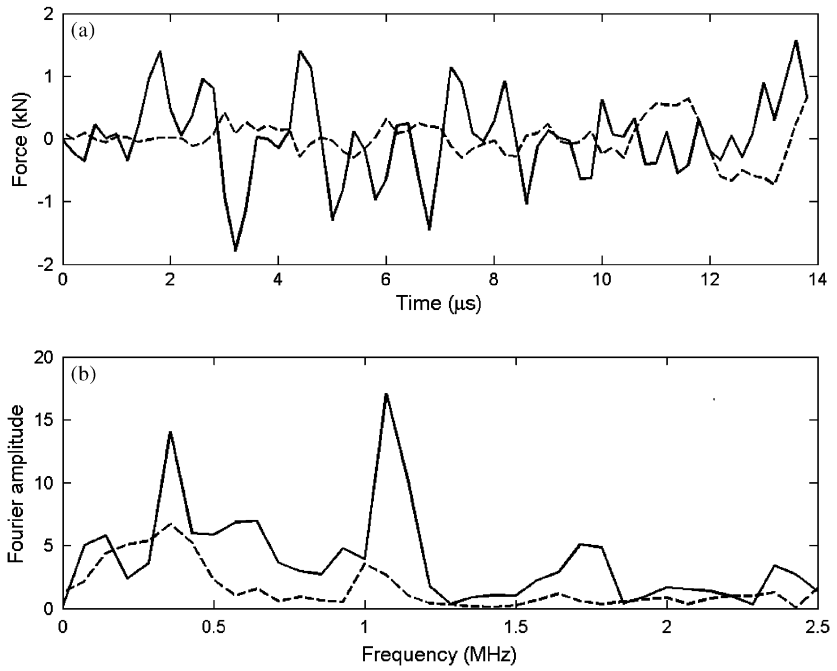

Fig. 13. (a) The force time function of the 3-D source due to the input signal with central frequency of 1 MHz and (b) the Fourier spectrum of the force time function.

the radial face, the axial force time function F_{axial} is expected to be larger in amplitude than the radial force time function F_{radial}, which is shown to be the case for each input signal. To determine how accurate the force time functions are for each case, the change in thickness and diameter calculated from the first peak input voltage can be compared to those calculated from the force from the first peak in the force time function, which corresponds to the first peak input voltage. The change in thickness Δh due to an input voltage V is

$$\Delta h = d_{33} V \tag{18}$$

and the change in diameter ΔD due to an input voltage V is

$$\Delta D = \frac{d_{31} D}{h} V, \tag{19}$$

where d_{33} and d_{31} are piezoelectric constants (Table 1). The changes in thickness and in diameter due to applied forces are obtained from the stress–strain relationship by converting the forces into stresses in the axial and radial directions. Adopting the abbreviated notations from Auld [24], the stress–strain relationship is

$$S_I = s_{IJ}^{E,C} T_J, \tag{20}$$

where S_I and T_J are strains and stresses and s_{IJ}^{E} and s_{IJ}^{C} are the compliances measured in constant electric field and in constant charge density, respectively (Table 1). Because of the coupling between electric and acoustic fields in the PZT disc, measurement of the mechanical properties depends on the electrical constraints [24]. The dynamic electric field within the PZT disc is unknown during the experiment, so the compliances measured in a constant electric field and in constant charge density are used to calculate the changes in thickness and in diameter. The results are tabulated in Table 2, where positive sign denotes extension and negative sign denotes contraction. For each input electric signal, the changes in thickness and in diameter calculated from the peak forces are larger than those calculated from the peak voltage. The discrepancies may be due to the fact that the simple calculations above assume idealized boundary conditions and static mechanical and electrical behavior, while the real behavior is dynamic; but the changes in thickness and diameter calculated from the peak forces and from the peak voltage are of the same order of magnitude. Also observed from the table is that the change in thickness is always larger than the change in diameter because the disc is excited axially. As expected, the larger the peak voltage, the larger the changes in thickness and in diameter, and this fact is also reflected in the calculation from the peak forces.

The dynamic mechanical behavior of the source can be studied from the waveform of the force time functions. The waveform of the force time functions from 0 to 4 μs looks quite similar to their respective input electric signals in Fig. 3 while the later part of all the force time functions oscillates with varying amplitudes at different frequencies. This is to be expected since the PZT disc is known to resonate due to electrical excitation, and the frequencies at which it resonates can be seen from the Fourier spectra of the force time functions. In all cases, it is apparent that three peaks in the Fourier spectra are at the same frequencies: 0.32, 1.1 and 1.7 MHz, while two peaks that occur at the same frequencies are not as apparent: 0.63 and 0.95 MHz.These results can be explained by the axial normal modes of the PZT disc, assuming axial faces are stress free. This assumption is acceptable because the disc is excited axially and the axial p-wave impedance of

Table 2
Deformation of the source calculated from the peak forces and peak voltage

Input electrical signal central frequency (MHz)	Peak axial force (N)	Peak radial force (N)	Change in thickness[E] (μm)	Change in thickness[C] (μm)	Change in diameter[E] (μm)	Change in diameter[C] (μm)
0.4	1240	−45	1.05	0.52	−0.81	−0.36
0.6	1720	−90	1.46	0.73	−1.16	−0.54
0.8	1560	−34	1.31	0.66	−0.98	−0.43
1	1400	−110	1.20	0.60	−1.00	−0.49

Input electrical signal central frequency (MHz)	Peak voltage (V)	Change in thickness (μm)	Change in diameter (μm)
0.4	346	0.13	−0.11
0.6	622	0.23	−0.20
0.8	586	0.22	−0.19
1	482	0.18	−0.15

[E]Calculated from compliances measured in constant electric field.
[C]Calculated from compliances measured in constant density charge.

piezoelectric solid ($\rho V_p = 29.3\,\text{MPa s/m}^3$) is almost three times higher than that of gypsum ($\rho V_{pa}^E = 11.0\,\text{MPa s/m}^3$), where V_{pa}^E is the axial p-wave velocity measured in a constant electric field. The axial normal modes are the solutions to the following equation:

$$\sin(\pi f_n h/V_{pa}) = 0, \quad \cos(\pi f_n h/V_{pa}) = 0, \tag{21}$$

which have solutions

$$f_n = nV_{pa}/2h, n = 1, 2, 3, \ldots, \tag{22}$$

where f_n are the normal modes, h is the thickness of the PZT disc and V_{pa} is the axial p-wave velocity. The first five modes observed from the Fourier spectra in Figs. 10–13 and the modes calculated from Eq. (22) with two different V_{pa} measured in a constant electric field and in constant charge density are tabulated in Table 3. Note that all five modes calculated from Eq. (22) are slightly smaller than those observed from the peaks in the Fourier spectra in all cases. The difference is expected since the actual boundary conditions of the disc are not truly stress free as in the calculations, and also there may be other modes in addition to the axial modes being excited.

The fitted data in Figs. 14–17 are obtained by convolving the Green's functions with the force time functions through Eq. (17). Since the inverse problem is overdetermined and is solved by least squares, the fitted data are not necessarily identical to the recorded data and so it is meaningful to compare them to examine the misfit. In each case, the fitted data have a good match with the original recorded data. There may be several sources that lead to the very slight misfit. First, the Green's function calculated based on Q damping may not truly capture the inhomogeneity in the gypsum plate and all the damping processes during wave propagation. Second, the Green's function is calculated assuming each sub-region is a point source, and the

Table 3
Axial normal modes of the PZT disc

	Modes (MHz)				
	$n=1$	$n=2$	$n=3$	$n=4$	$n=5$
Calculated from normal mode theory[E]	0.26	0.53	0.79	1.1	1.3
Calculated from normal mode theory[C]	0.30	0.61	0.91	1.2	1.5
Observed from the Fourier spectra of the force time functions	0.32	0.63	0.95	1.1	1.7

[E]Calculated from axial *p*-wave velocity measured in constant electric field (see Table 1).
[C]Calculated from axial *p*-wave velocity measured in constant density charge (see Table 1).

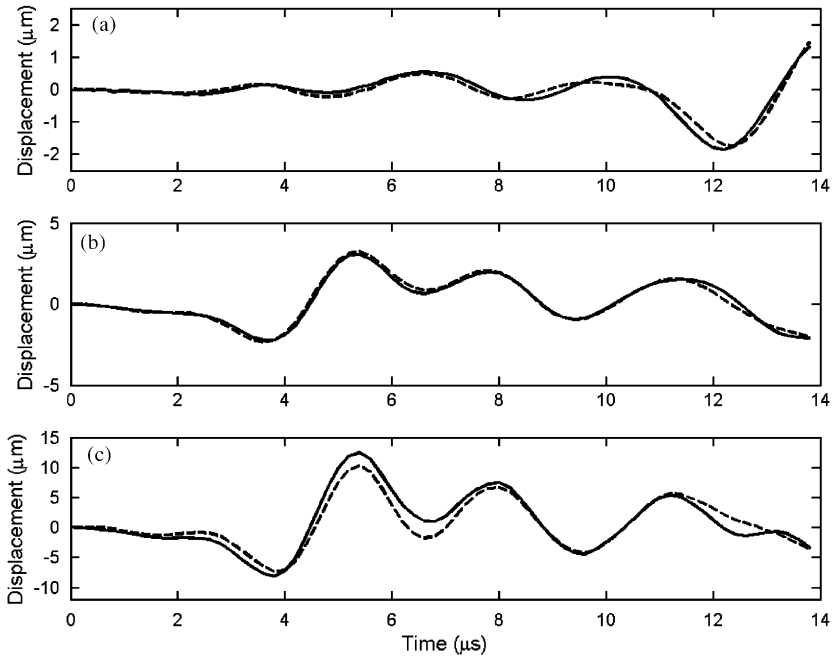

Fig. 14. Comparison of recorded signals due to the input signal with central frequency of 400 kHz and the fitted data from the inversion. (a) sensor 1, (b) 2, (c) 3. ——, recorded data; - - - -, filled data.

error in the Green's function grows with increasing frequency [7]. However, from the good match between the fitted data and the recorded data, these errors are deemed to be minor.

The very long computation time (47 consecutive days) used to calculate all the Green's functions raises the question of the practicality of the current method. The computation can be made more efficient by a change of platform and integration algorithm. Since the current code is in written in Matlab running in Windows 2000, it is believed that the computation time can be reduced by well more than 50% if the code were written in Fortran or in C running on a Linux platform. In addition, the numerical integration of the wavenumber integral in Kennett's method

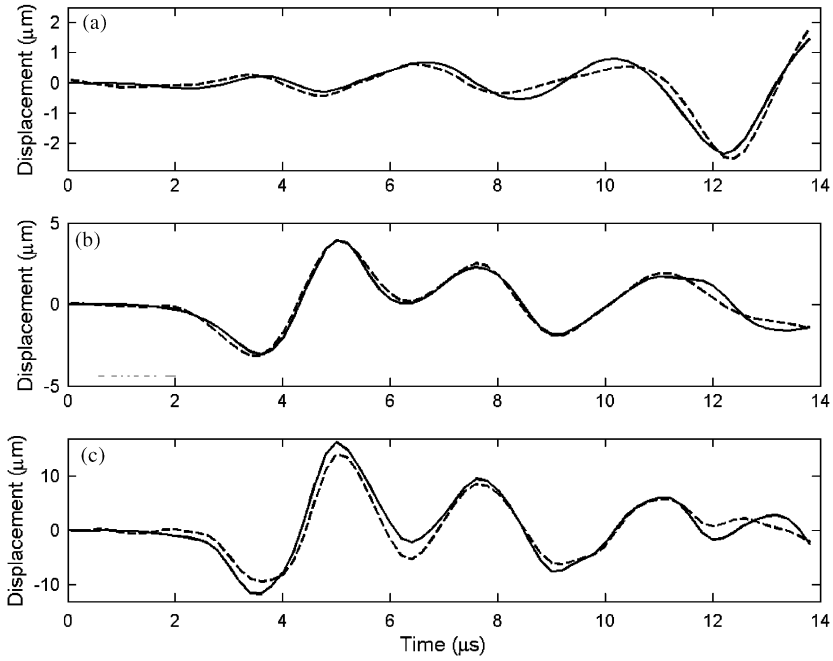

Fig. 15. Comparison of recorded signals due to the input signal with central frequency of 600 kHz and the fitted data from the inversion. (a) sensor 1, (b) 2, (c) 3. ——, recorded data; - - - -, filled data.

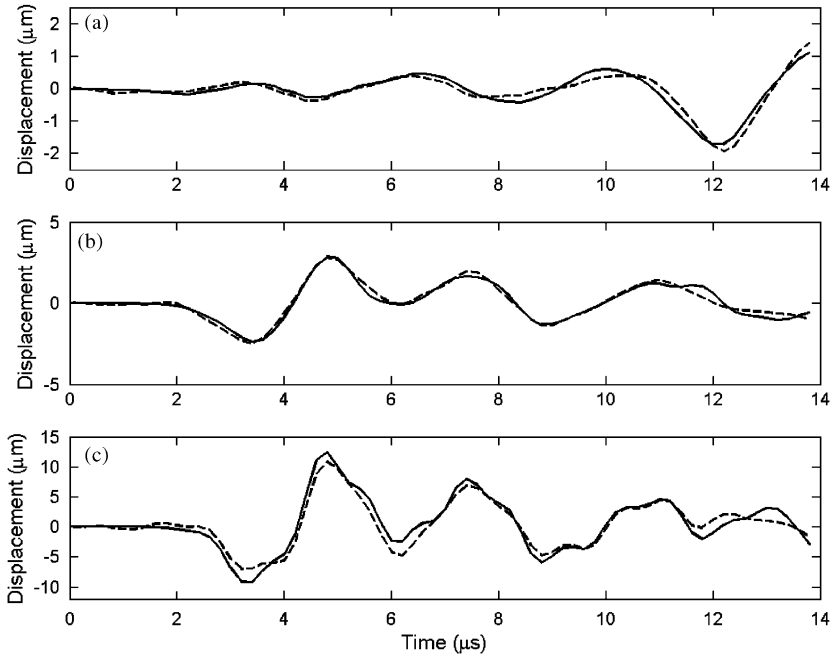

Fig. 16. Comparison of recorded signals due to the input signal with central frequency of 800 kHz and the fitted data from the inversion. (a) sensor 1, (b) 2, (c) 3. ——, recorded data; - - - -, fitted data.

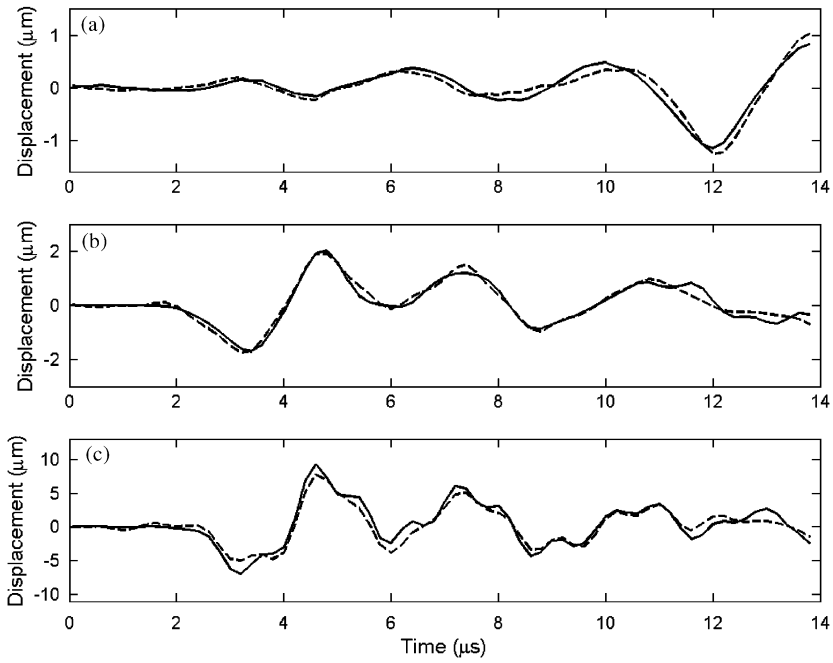

Fig. 17. Comparison of recorded signals due to the input signal with central frequency of 1 MHz and the fitted data from the inversion. (a) sensor 1, (b) 2, (c) 3. ——, recorded data; - - - -, filled data.

[20] is performed by Simpson's rule. A more efficient scheme can be developed by approximating the integrand by Chebyshev polynomials as performed by Xu and Mal [25], but this requires some testing to make the method work well. A new Windows-based computer will nominally run about five times faster than the older machine used for this paper.

7. Conclusions

In this study, we have successfully used theoretical Green's functions incorporating Q damping to perform a full waveform inversion. There are three crucial factors that we believe lead to the successful inversion: (1) the use of broadband transducers with high-fidelity frequency response, (2) the use of Green's functions based on Q damping, and (3) taking the source finiteness into account. The use of narrowband transducers requires obtaining the transfer function each time a test is performed on a different solid and then performing deconvolution of the microseismic data from the transfer function. Since a narrowband transducer has missing data in some frequencies, the deconvolution is fundamentally ill-posed. For broadband transducers, all displacement information present is being transduced and is included in the inversion.

The microseismic data are inverted from inelastic Green's functions, rather than based on a linear, homogenous, elastic solid model. For a plate, Q can be obtained experimentally by

breaking a capillary on one side of the plate. It captures the damping behavior of the gypsum quite well.

This study also incorporates the source finiteness in formulating the inverse problem. Since the source size is known a priori, the disc can be discretized into subregions with the largest dimension less than the minimum wavelength such that each subregion is effectively a point source. This is believed to improve the accuracy of the Green's functions and consequently lead to better inversion results.

The success of a full waveform inversion is judged by whether the inverted results can be explained physically. The inverted force time functions match the known mechanical behavior of the PZT disc and the observed oscillations match well with the theoretical axial normal modes.

Although the use of high–fidelity sensors, the calculation of the Green's function that includes damping, the summation of point sources into finite sources, and the technique of inversion are each not new, the incorporation of all the above to obtain physically justified source time functions for a complex source is a new development in microseismic inversion. It should be emphasized that in this study the source time function is not parametrized a priori like many seismologists and acoustic emission researchers do nowadays to obtain physical solutions. For dynamic crack inversion, it is certainly fine to assume the waveform of the source time function to be a step function. In more complicated dynamic processes such as in this study, direct deconvolution must be used to determine the source processes. In fact, recently the source time function on a subfault calculated based on an asperity model for dynamic earthquake faulting shows more than a step function: the source time function is actually a step function, followed by periodic undulations [26]. If the parameterization of a step function is used for inversion, the real behavior of the source process will not be obtained. Another problem associated with the parameterization of the source time function is that the inversion problem becomes nonlinear and will always involve more complicated algorithms to solve the problem. In conclusion, this study demonstrates the feasibility of obtaining the most complete and physically justified quantitative information from a dynamic source process in a damped solid.

Acknowledgements

This research is supported by NSF project CMS-9908218, 'Multi-Scale Experimental Investigation of Sliding Friction.'

References

[1] C.B. Scruby, G.R. Baldwin, K.A. Stacey, Characterisation of fatigue crack extension by quantitative microseismic, *International Journal of Fracture* 28 (1985) 201–222.

[2] C.B. Scruby, K.A. Stacey, G.R. Baldwin, Defect characterisation in three dimensions by acoustic emission, *Journal of Physics D: Applied Physics* 19 (1986) 1597–1612.

[3] M. Ohtsu, Simplified moment tensor analysis and unified decomposition of acoustic emission source: application to in situ hydrofracturing test, *Journal of Geophysical Research* 96 (1991) 6211–6221.

[4] F.R. Breckenridge, T.M. Proctor, N.N. Hsu, S.E. Fick, D.G. Eitzen, Transient sources for acoustic emission work, *Procceedings of the 10th International Acoustic Emission Symposium*, Tokyo, 1990, pp. 20–37.

[5] J.E. Michaels, T.E. Michaels, W. Sachse, Applications of deconvolution to microseismic signal analysis, *Materials Evaluation* 39 (1981) 1032–1036.
[6] S.D. Glaser, P.P. Nelson, Acoustic emissions produced by discrete fracture in rock—part 2: kinematics of crack growth during controlled Mode I and Mode II loading of rock, *International Journal of Rock Mechanics* 29 (1992) 253–265.
[7] T. Lay, T. Wallace, *Modern Global Seismology*, first ed, Academic Press, San Diego, 1995.
[8] B.W. Stump, L.R. Johnson, The determination of source properties by the linear inversion of seismograms, *Bulletin of the Seismological Society of America* 67 (1977) 1489–1502.
[9] R.A. Strelitz, Moment tensor inversions and source models, *Geophysical Journal of the Royal Astronomical Society* 52 (1978) 359–364.
[10] K.Y. Kim, W. Sachse, Acoustic emissions from penny-shaped cracks in glass—part II: Moment tensor and source–time function, *Journal of Applied Physics* 59 (1986) 2711–2715.
[11] K.Y. Kim, W. Sachse, Characteristics of an microseismic source from a thermal crack in glass, *International Journal of Fracture* 31 (1986) 211–231.
[12] M. Enoki, T. Kishi, Theory and analysis of deformation moment tensor due to microcracking, *International Journal of Fracture* 38 (1988) 295–310.
[13] K.R. Shah, J.F. Labuz, Damage mechanisms in stressed rock from acoustic emission, *Journal of Geophysical Research* 100 (1995) 15527–15539.
[14] T. Kishi, M. Ohtsu, S. Yuyama (Eds.), *Acoustic Emission—Beyond the Millennium*, Elsevier, New York, NY, 2000.
[15] S.H. Hartzell, T.H. Heaton, Inversion of strong ground motion and teleseismic waveform data for the fault rupture history of the 1979 Imperial Valley, California, earthquake, *Bulletin of the Seismological Society of America* 73 (1983) 1553–1583.
[16] J.E. Michaels, Y.H. Pao, The inverse problem for an oblique force on an elastic plate, *Journal of the Acoustical Society of America* 77 (1985) 2005–2011.
[17] S.D. Glaser, G. Weiss, L.R. Johnson, Body waves recorded inside an elastic half space by an embedded wideband velocity sensor, *Journal of the Acoustical Society of America* 104 (1998) 1404–1412.
[18] K. Aki, P.G. Richards, *Quantitative Seismology, Theory and Method*, second ed., University Science Books, Sausalito, CA, 2000.
[19] E. Kjartansson, Constant Q-wave propagation and attenuation, *Journal of Geophysical Research* 84 (1979) 4737–4748.
[20] B.L.N. Kennett, *Seismic Wave Propagation in Stratified Media*, Cambridge University Press, Cambridge, UK, 1983.
[21] M. Niazi, L.R. Johnson, Q in the inner core, *Physics of the Earth and Planetary Interiors* 74 (1992) 55–62.
[22] L. Knopoff, *Q, Review of Geophysics* 2 (1964) 625–660.
[23] R. Apsel, Dynamic Green's functions for layered media and applications to boundary-value problems, *Ph.D. Thesis*, University of California, San Diego, 1979.
[24] B.A. Auld, *Acoustic Fields and Waves in Solids (two volumes)*, second ed., Krieger Publications, Florida, 1990.
[25] P. Xu, A.K. Mal, An adaptive integration scheme for irregularly oscillatory functions, *Wave Motion* 7 (1985) 235–243.
[26] L.R. Johnson, R. Nadeau, An asperity model of an earthquake: dynamic problem, *Bulletin of the Seismological Society of America*, in press.